Duty Cycle Control Set Model Predictive DC-Link Voltage Control Method for PMSM Film-Capacitor-Driven System

Zhenrui ZHANG, Jing XU, Xinyu WANG, and Qingya ZHANG

***Abstract*—This paper proposes a robust duty cycle control set model predictive DC-link voltage control (DCS-MPDVC) to suppress the DC-link voltage oscillations in the permanent magnet synchronous motor (PMSM) film-capacitor drive system. This method applies an extended state observer (ESO) to suppress unmodeled disturbances and parameter variations and estimate the inductor current of the inverter. Subsequently, to ensure the constraint accuracy of the *dq*-axis current and DC-link voltage, a discrete duty cycle control set is constructed to reduce the prediction error within each control cycle. In addition, a sector judgment mechanism for voltage vector selection is introduced to reduce the computational complexity while maintaining the control performance. The proposed control strategy is experimentally verified on a film-capacitor hardware test platform using DSP, demonstrating the effectiveness of DCS-MPDVC in suppressing the DC-link voltage and optimizing the computational efficiency.**

***Index Terms*—Duty cycle control set system, extended state observer, oscillation suppression, permanent magnet synchronous motor.**

I. Introduction

THE film-capacitor driven system for permanent-magnet synchronous motors has recently been applied in industrial appliances like air-conditioners and aircraft propulsion systems due to its high-efficiency, high-power-density, and low-failure-rate advantages [1], [2]. However, reducing the capacitance value of the DC-link capacitor leads to DC-link voltage oscillations [3]. Active damping compensation based on vector control is an effective control method to tackle this issue. But, it can only passively maintain system stability by increasing damping [4]–[6]. Therefore, to address the adverse effects of DC-link voltage disturbances on the system, direct constraints are imposed on it to achieve better steady-state performance of the motor. For example, designing a DC-link voltage prediction equation and cost function using finite-control-set model predictive control (FCS-MPC) can achieve multi-objective optimization for the film-capacitor-driven system [7]. The constraint on the DC-link voltage can also be incorporated as an additional optimization objective in the cost function of FCS-MPC to achieve stability in the film-capacitor drive system [8]. The stability of FCS-MPC applied to the film-capacitor system has been demonstrated in [9]. A DC-link current observer has been developed in [10] to minimize sensor reliance. However, the accuracy of the predictive equation and control set limits the effectiveness of the constraint on the DC-link voltage. Some solutions have been proposed to address the control and prediction-accuracy issues of the electrolytic-capacitor system [11].

Motor parameter identification [12] and prediction error compensation [13] can solve the system problem of time-varying parameters. However, chip performance will affect their compensation effect, and these methods cannot solve the problem of inaccurate motor modeling. Compared with these schemes, it is simpler and more efficient to use disturbance observers (such as Luenberger observer [14], [15], extended Kalman filter [16], sliding mode observer [17], and adaptive observer [18]) to solve the problems of time-varying parameters and inaccurate modelling. Meanwhile, the disturbance observer not only observes the disturbance of the system but also simplifies the design of the predictive controller. Professor Han proposed anti-disturbance control technology and ESO [19], which can effectively reduce the impact of inaccurate mathematical modelling on the controller. The ESO can extend the unknown part of the motor modelling to an independent state variable and observe it to achieve the real-time acquisition of the motor state [20]. The ESO has more anti-disturbance and parameter-tuning advantages than the traditional disturbance observer. Based on the ESO, progress has also been made in reducing parameter disturbance. [21], [22] have utilized the ESO to develop an accurate prediction model. However, these methods are based on deadbeat model predictive control (MPC). Due to the absence of an explicit cost function, DC-link voltage constraints cannot be added, rendering these methods unsuitable for directly suppressing DC-link voltage oscillation.

When there is only a current prediction equation, solving the

Manuscript received July 29, 2025; accepted August 15, 2025. Date of publication December 30, 2025; date of current version September 9, 2025. This work was supported by the National Natural Science Foundation of China under the grant 51979021 and 51905229, Jiangsu University of Science and Technology Doctoral Research Start-up Funds under the grant 1172932302, and Basic science (Natural science) Research Project of Higher Education in Jiangsu Province under the grant 24KJD470004. (*Corresponding authors: Zhenrui Zhang.*)

All authors are with the Department of Marine Equipment and Technology Institute, Jiangsu University of Science and Technology, Zhenjiang 212003, China (e-mail: tabz00@qq.com, xujing@just.edu.cn, 202200000212@just.edu.cn, 202200000207@just.edu.cn).

Digital Object Identifier 10.24295/CPSSTPEA.2025.00029

deadbeat method can consider both steady-state performance and solution accuracy. However, the multi-objective optimization system has a coupling problem, and the control law cannot be solved directly. Therefore, it is necessary to solve the cost function online. Limited by the controller's performance, the finite control set method is mainly used for the solution. However, the control accuracy of the basic control set relying on the inverter switching state is challenging to meet the control requirements. In order to address this issue, a method proposed in [23] reduces the amplitude of six fundamental effective vectors to half of their original value. It combines two adjacent voltage vectors into a new vector. This approach expands the control set of voltage vectors, resulting in 20 voltage vectors and improved control accuracy. In [24], virtual vectors with different phase angles are generated by averaging the included angles of adjacent fundamental effective vectors, leading to an extended vector control set. This scheme effectively enhances the control accuracy of the vector phase angle. However, significant current ripple still exists at low speeds due to the large vector amplitude. [25] addresses this issue by selecting the optimal voltage vector through multiple iterations of voltage amplitude and angle. However, this approach requires considerable computational resources and is typically applied to high-performance chips such as FPGAs. Using the deadbeat method for duty cycle calculation can lead to performance degradation due to potential changes in motor parameters during operation [26], [27]. On the other hand, a discrete duty cycle is a control set design scheme that exhibits robustness [28], but it lacks an optimization strategy to improve algorithm efficiency. Therefore, further investigation and research are required to explore optimized control strategies for improving the constraint on the DC-link voltage.

This paper introduces the DCS-MPDVC for film capacitor PMSM drive systems to balance control accuracy and computational burden. This approach offers two key contributions:

1) Given the positive correlation between the predicted DC-link voltage and the predicted *dq*-axis currents, an anti-disturbance prediction model for DC-link voltage is developed based on the ESO to improve the prediction accuracy of the DC-link voltage and estimate the inductor current of the inverter. Meanwhile, an under-damped parameter allocation method is introduced and combined with a low-pass filter to enhance the observation accuracy, thus saving the hardware configuration of physical sensors.

2) A duty cycle control set is put forward to decrease the prediction errors associated with the DC-link voltage and *dq*-axis currents. Meanwhile, a sector judgment mechanism and a design method for the duty cycle control set are presented. In a single prediction process, the constraints on the DC-link voltage and *dq*-axis currents are strengthened by comprehensively applying optimal and sub-optimal basic voltage vectors.

This study validates the algorithm's effectiveness in reducing current ripple and suppressing voltage oscillation through a surface-mounted PMSM (SPMSM) film-capacitor drive setup. The paper is structured as follows: The basic design principle of the anti-disturbance prediction model and the method for configuring observer parameters are presented in Section II. Section III discusses the design principles of the duty cycle control set and sector judgment mechanism. Section IV focuses on conducting experimental verification, validating the advantages of the duty cycle control set, the observer, and the suppression of DC-link voltage oscillation.

II. Design and Analysis of Robust Model Predictive DC-Link Voltage Control

The current predictive controller of PMSM ignores the nonlinearity of the inverter and time-varying parameters. Therefore, this study uses the ESO methodology to design a predictive DC-link voltage model.

A. SPMSM's Current Mathematical Model

The accurate mathematical model of SPMSM in a rotating coordinate system can be expressed by

$$\begin{cases} \dfrac{\mathrm{d}i_d}{\mathrm{d}t} = -\dfrac{R_\mathrm{s}+\Delta R_\mathrm{s}}{L_\mathrm{s}+\Delta L_\mathrm{s}} i_d + \omega_\mathrm{e} i_q + \dfrac{1}{L_\mathrm{s}+\Delta L_\mathrm{s}} v_d + f_d \\ \dfrac{\mathrm{d}i_q}{\mathrm{d}t} = -\dfrac{R_\mathrm{s}+\Delta R_\mathrm{s}}{L_\mathrm{s}+\Delta L_\mathrm{s}} i_q - \omega_\mathrm{e}\left(i_d + \dfrac{\psi+\Delta\psi}{L_\mathrm{s}+\Delta L_\mathrm{s}} \right) + \dfrac{1}{L_\mathrm{s}+\Delta L_\mathrm{s}} v_q + f_q \end{cases} \tag{1}$$

where, i_d, i_q, v_d, and v_q are the motor's current and voltage in the rotating coordinate system(*dq*-axis). R_s is the motor's phase resistance. L_s are the SPMSM's inductance in the *dq*-axis. ω_e is the motor's electric angular velocity. ψ is the flux linkage of the permanent magnet. f_d and f_q represent the unknown disturbance in the *dq*-axis. The "Δ" represents the error between the motor's actual and controller parameters.

The PMSM current model in (1) is divided into two parts: the input and the lumped disturbance, as shown in

$$\begin{cases} \dot{\boldsymbol{i}}_\mathbf{s} = \boldsymbol{I}_\mathrm{f} + b\boldsymbol{v}_\mathrm{s} \\ \boldsymbol{Y} = \boldsymbol{i}_\mathbf{s} \\ \boldsymbol{I}_\mathrm{f} = \begin{bmatrix} i_{d\mathrm{f}} \\ i_{q\mathrm{f}} \end{bmatrix} = \begin{bmatrix} -\dfrac{R_\mathrm{s}+\Delta R_\mathrm{s}}{L_\mathrm{s}+\Delta L_\mathrm{s}} i_d + \omega_\mathrm{e} i_q + f_d \\ -\dfrac{R_\mathrm{s}+\Delta R_\mathrm{s}}{L_\mathrm{s}+\Delta L_\mathrm{s}} i_q - \omega_\mathrm{e} i_d - \omega_\mathrm{e}\dfrac{\psi+\Delta\psi}{L_\mathrm{s}+\Delta L_\mathrm{s}} + f_q \end{bmatrix} \end{cases} \tag{2}$$

where, $\boldsymbol{i}_\mathrm{s} = [i_d, i_q]^\mathrm{T}$, $\boldsymbol{v}_\mathrm{s} = [v_d, v_q]^\mathrm{T}$. b is regarded as the gain of the input value, and the current gain of the *d*-axis and *q*-axis of SPMSM is regarded as the same value. $\boldsymbol{I}_\mathrm{f}$ is a nonlinear current disturbance term.

B. Design of Disturbance Observer

The anti-disturbance predictive model adopts the ESO to estimate the motor's lumped disturbance. The disturbance value of the system model can be observed through the input and output of the system. Firstly, the observer model is established according to (2),

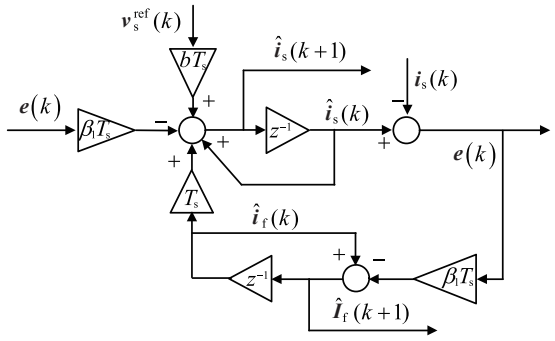

Fig. 1. The disturbance observer computation structure.

$$\begin{cases} \boldsymbol{e} = \hat{\boldsymbol{i}}_s - \boldsymbol{i}_s \\ \dot{\hat{\boldsymbol{i}}}_s = \hat{\boldsymbol{I}}_f + b\boldsymbol{v}_s - \beta_1 \boldsymbol{e} \\ \dot{\hat{\boldsymbol{I}}}_f = -\beta_2 \boldsymbol{e} \end{cases} \tag{3}$$

where, $\boldsymbol{e} = [e_d, e_q]^T$, $\hat{\boldsymbol{i}}_s = [\hat{i}_d, \hat{i}_q]^T$, $\hat{\boldsymbol{I}}_f = [\hat{i}_{df}, \hat{i}_{qf}]^T$.

After the Laplace transform, use (3) to calculate the transfer function of actual disturbance $\boldsymbol{I}_f$ and estimated disturbance $\hat{\boldsymbol{I}}_f$:

$$\hat{\boldsymbol{I}}_f = \beta_2 \frac{\boldsymbol{i}_s s - b\boldsymbol{v}_s}{s^2 + s\beta_1 + \beta_2} = \beta_2 \frac{\boldsymbol{I}_f}{s^2 + s\beta_1 + \beta_2} \tag{4}$$

(4) can be set through parameter configuration as a low-pass filter with a bandwidth ω_f. The transfer function of the second-order low-pass filter is

$$G(s) = \frac{\hat{\boldsymbol{I}}_f}{\boldsymbol{I}_f} = \frac{1}{\frac{s^2}{\omega_f^2} + 2\xi\frac{s}{\omega_f} + 1} \tag{5}$$

After comparing (5) with (4), $\beta_2 = \omega_f^2$, $\beta_1 = 2\omega_f\xi$, the damping coefficient ξ is set to 0.707 by using the design method of the Butterworth filter. The parameter configuration method based on the low-pass filter can be defined as:

$$\begin{cases} \beta_2 = \omega_f^2 \\ \beta_1 = 1.414\omega_f \end{cases} \tag{6}$$

Configure an observation bandwidth larger than the lumped disturbance to estimate the actual disturbance effectively.

C. DC-Link Voltage Anti-Disturbance Prediction Equation

The observer's discrete is obtained by the forward Euler expansion of (3). The control structure of the current disturbance observer is shown in Fig. 1.

$$\begin{cases} \boldsymbol{e}(k) = \hat{\boldsymbol{i}}_s(k) - \boldsymbol{i}_s(k) \\ \hat{\boldsymbol{i}}_s(k+1) = T_s[\hat{\boldsymbol{I}}_f(k) + b\boldsymbol{v}_s^{ref}(k) - \beta_1\boldsymbol{e}(k)] + \boldsymbol{i}_s(k) \\ \hat{\boldsymbol{I}}_f(k+1) = \hat{\boldsymbol{I}}_f(k) - T_s\beta_2\boldsymbol{e}(k) \end{cases} \tag{7}$$

The current disturbance $\boldsymbol{I}_f$ of the motor observed through (3) is brought into (2) to obtain an accurate motor current model. Then, according to the basic principle of FCS-MPC and the inverter basic voltage vectors $\boldsymbol{v}_s^{ref}$, the prediction equation is obtained by forward Euler expansion based on the sample time T_s.

$$\boldsymbol{i}_s(k+1) = T_s[\boldsymbol{I}_f(k) + b\boldsymbol{v}_s^{ref}] + \boldsymbol{i}_s(k) \tag{8}$$

Two-step prediction is adopted to obtain the predicted value of the $k+2$ control cycle because of the one-step control delay of the chip controller.

$$\boldsymbol{i}_s(k+2) = T_s[\hat{\boldsymbol{I}}_f(k+1) + b\boldsymbol{v}_s^{ref}] + \hat{\boldsymbol{i}}_s(k+1) \tag{9}$$

The current disturbance observer has very high observation accuracy and low observation error, namely $\boldsymbol{i}_s(k+1) \approx \hat{\boldsymbol{i}}_s(k+1)$, $\boldsymbol{I}_s(k+1) \approx \hat{\boldsymbol{I}}_s(k+1)$. Therefore, $\hat{\boldsymbol{I}}_f(k+1)$ and $\hat{\boldsymbol{i}}_s(k+1)$ can be obtained by the observer.

The current predictive equation is designed by (9). The predicted value of different basic voltage vectors is obtained through the prediction equation, and the predicted value is compared with the current reference value to obtain the cost function in (10). And constraints related to current limits can also be incorporated in

$$g = [i_d^{ref} - i_d(k+2)]^2 + [i_q^{ref} - i_q(k+2)]^2 \tag{10}$$

In (10), i_d^{ref} and i_q^{ref} are the dq-axis current reference values, which are usually calculated through the speed loop. g represents the prediction error. The voltage vector contained in the control set is brought in (10) individually to obtain the cost value (prediction error). The minimal prediction error g_{min} corresponds to the optimal voltage vector.

The topology structure is depicted in Fig. 2. The voltage equation of the DC-link is given by

$$C\frac{\mathrm{d}v_{dc}}{\mathrm{d}t} = i_L - i_{dc} \tag{11}$$

where, C is the capacitor value. i_L is the inductor current. i_{dc} is the DC-link current, and v_{dc} is the DC-link voltage.

The analysis can be carried out for (11), and the corresponding ESO shown in (12) can be established to observe the inductor current.

$$\begin{cases} e(k) = \hat{v}_{dc}(k) - v_{dc}(k) \\ \hat{v}_{dc}(k+1) = T_s\left[\frac{\hat{i}_L(k)}{C} - \frac{i_{dc}(k)}{C} - \beta_1 e(k)\right] + \hat{v}_{dc}(k) \\ \hat{i}_L(k+1) = -T_s\beta_2 e(k) + \hat{i}_L(k) \end{cases} \tag{12}$$

i_{dc} can be obtained from the equivalent formula of the inverter (using the control strategy of $i_d = 0$).

$$i_{dc}(k+2) = \frac{3v_q(k)\hat{i}_q(k+2)}{2v_{dc}(k)} \tag{13}$$

Based on the ESO for inductor current, the predicted current value, delay compensation, and the estimated applied voltage are combined to estimate the DC-link current of the following control cycle. (14) is used to predict the DC-link voltage.

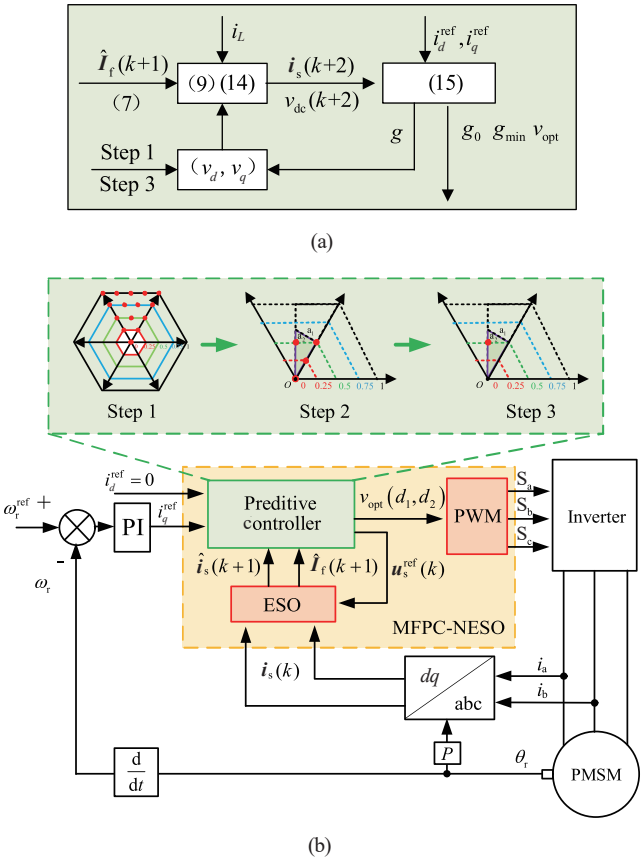

Fig. 2. DCS-MPDVC control structure diagram. (a) Predictive controller, (b) Overall control structure diagram.

$$\begin{cases} v_{\mathrm{dc}}(k+2) = v_{\mathrm{dc}}(k) + \dfrac{1}{C}\left[i_L(k) - i_{\mathrm{dc}}(k+2)\right] T_{\mathrm{s}} \\ i_{\mathrm{dc}}(k+2) = \dfrac{3\left[\hat{i}_d(k+2)v_d^{\mathrm{ref}}(k) + \hat{i}_q(k+2)v_q^{\mathrm{ref}}(k)\right]}{2v_{\mathrm{dc}}(k)} \end{cases} \tag{14}$$

As shown in (14), i_{dc} needs to be calculated using the motor current equation. Therefore, the accuracy of the current equation is essential for predicting the DC-link voltage.

The cost function of DC-link voltage control is [29]

$$\begin{cases} g_{\mathrm{dc}} = g + k_{\mathrm{v}}\left[v_{\mathrm{dc}}^{\mathrm{ref}} - v_{\mathrm{dc}}(k+2)\right]^2 \\ k_{\mathrm{v}} = \dfrac{I_{\mathrm{N}}^2}{V_{\mathrm{dc}}^2} \end{cases} \tag{15}$$

Furthermore, to ensure the system's stability, it is necessary to analyze its damping characteristics. The system damping is directly related to the control voltage. Given that the control strategy of $i_d = 0$ is adopted, the damping compensation related to the q-axis voltage is mainly considered. Therefore, the q-axis reference voltage value needs to be analyzed according to (15). Here, the cost function in the steady state is considered, and its partial derivative is taken to obtain the extreme value solution. First, when the voltage constraint is not added, the partial derivative of the cost function with respect to the q-axis voltage is:

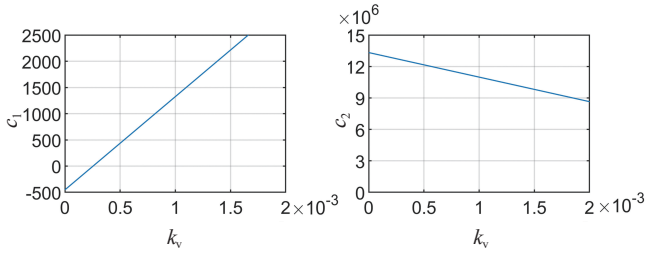

Fig. 3. The curve of system eigenvalues changing with k_{v}.

$$\frac{\partial g}{\partial v_q} = \frac{2T_{\mathrm{s}}^2 v_q}{L_q^2} - \frac{2T_{\mathrm{s}}\left(i_{q\mathrm{ref}} - i_q + \dfrac{R_{\mathrm{s}}T_{\mathrm{s}}i_q}{L_q} + \dfrac{\psi T_{\mathrm{s}}\omega_{\mathrm{e}}}{L_q}\right)}{L_q} \tag{16}$$

k_{v} is used to represent the weight coefficient of the voltage constraint term g_{v}, then the partial derivative of it concerning the q-axis voltage is:

$$\frac{\partial g_{\mathrm{v}}}{\partial v_q} = -\frac{3T_{\mathrm{s}}i_q k_{\mathrm{v}}\left(v_{\mathrm{dc}} - v_{d\mathrm{cref}} + \dfrac{T_{\mathrm{s}}i_L}{C} - \dfrac{3T_{\mathrm{s}}i_q v_q}{2Cv_{\mathrm{dc}}}\right)}{Cv_{\mathrm{dc}}} \tag{17}$$

Adding these two partial derivatives and setting the sum equal to zero allows us to obtain the analytical solution of the q-axis voltage corresponding to the extreme value of the cost function. At the same time, it is easy to prove that this solution is a minimum value by calculating the second-order partial derivative. Therefore, the q-axis voltage with voltage constraint can be expressed as

$$\begin{aligned} v_{q\_\mathrm{damp}} = {} & \frac{2T_{\mathrm{s}}}{L_q}\left(i_{q\mathrm{ref}} - i_q + \frac{R_{\mathrm{s}}T_{\mathrm{s}}i_q}{L_q} + \frac{\psi T_{\mathrm{s}}\omega_{\mathrm{e}}}{L_q}\right) \\ & + \frac{3T_{\mathrm{s}}i_q k_{\mathrm{v}}\left(v_{\mathrm{dc}} - v_{d\mathrm{cref}} + \dfrac{T_{\mathrm{s}}i_L}{C}\right)}{\dfrac{Cv_{\mathrm{dc}}}{L_q^2} + \dfrac{9T_{\mathrm{s}}^2 i_q^2 k_{\mathrm{dc}}}{2C^2 v_{\mathrm{dc}}^2}} \end{aligned} \tag{18}$$

After that, the inverter current value after applying the voltage constraint can be obtained by

$$\begin{aligned} i_{\mathrm{dc\_damp}} &\approx i_{\mathrm{dc}} + k_{\mathrm{v}}\frac{9L_q^2 I_q^2}{2CT_{\mathrm{s}}V_{\mathrm{dc}}^2}\tilde{v}_{\mathrm{dc}} + k_{\mathrm{v}}\frac{9L_q^2 I_q^2}{2C^2 V_{\mathrm{dc}}^2}i_L \\ &\triangleq i_{\mathrm{dc}} + a\tilde{v}_{\mathrm{dc}} + bi_L \end{aligned} \tag{19}$$

Subsequently, by using the eigenvalue analysis method [9] of traditional active-damping compensation, the characteristic equation of the system can be obtained:

$$s^2 + \underbrace{\left(\frac{a - P_L/V_{\mathrm{dc}}^2}{CV_{\mathrm{dc}}^2} + \frac{R_L}{L}\right)}_{c_1}s + \underbrace{\frac{\left[R_L\left(V_{\mathrm{dc}}^2 a - P_L\right) - V_{\mathrm{dc}}^2(b-1)\right]}{V_{\mathrm{dc}}^2 CL}}_{c_2} = 0 \tag{20}$$

Next, analyze the variation of two important stability coefficients c_1 and c_2, under rated conditions as k_{v} increases based on the motor parameters, as shown in Fig. 3. To a certain extent,

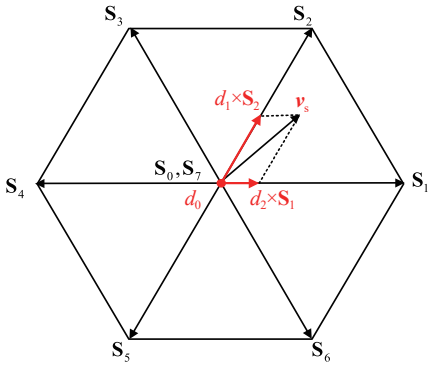

Fig. 4. The relationship between the optimal and suboptimal voltage vectors based on the duty cycle.

the value of c_2 is much greater than zero. So, the instability factor of the system is mainly reflected in the eigenvalue c_1. When $k_v = 0$, the characteristic coefficient of the system is negative, indicating that the system will oscillate. As k_v increases, when k_v is greater than the weight coefficient of the DC-link voltage constraint, the value of c_1 gradually shows a trend greater than zero. Therefore, the MPDVC plays the same role as the traditional active damping method in reshaping the damping and realizes the system's stable control from the active damping perspective.

Next, the key is to find out how to obtain the extreme value that makes the cost function zero. Since the optimization algorithm has a large amount of calculation, the burden on the motor controller is heavy. Therefore, the discrete control set is currently more mainstream. This paper proposes a high-efficiency optimization method based on the duty cycle discretization.

III. Design and Analysis of Duty Cycle Control Set

The voltage vector set used in FCS-MPC consists of fundamental voltage vectors determined by the inverter's output state, which directly corresponds to the motor's operational state. The utilization of inverter voltage plays a crucial role in minimizing prediction errors, particularly at low speeds, where the impact on current and DC-link voltage is more pronounced due to the significant difference in magnitude between the motor voltage vectors and the fundamental vectors. Therefore, optimizing the selection of voltage vectors in FCS-MPC is essential. This study proposes the inclusion of suboptimal voltage vectors alongside the optimal ones and introduces the duty cycle control set to synthesize virtual voltage vectors. This approach enables precise control with a negligible increase in computational load.

A. Duty Cycle Control Set Design

The basic voltage vector ($\mathbf{S}_i$, $i = 0 - 7$) of the two-level voltage source inverter is shown in Fig. 4. Assume the reference voltage vector at the control cycle is $\boldsymbol{v}_s$. One method uses the two adjacent basic vectors to synthesize this vector. Meanwhile, the duty cycle must be added to control the action time of these vectors. Then, in Fig. 4, the action time of $\mathbf{S}_2$ is d_2, and

TABLE I
Voltage Vector of Two-Level Voltage Source Inverter

S_i, i =	S_a	S_b	S_c	$v_{i,\alpha}$	$v_{i,\beta}$
0	0	0	0	0	0
1	1	0	0	$2v_{dc}\,d_i/3$	0
2	1	1	0	$v_{dc}\,d_i/3$	$\sqrt{3}v_{dc}\,d_i/3$
3	0	1	0	$-v_{dc}\,d_i/3$	$\sqrt{3}v_{dc}\,d_i/3$
4	0	1	1	$-2v_{dc}\,d_i/3$	0
5	0	0	1	$-v_{dc}\,d_i/3$	$-\sqrt{3}v_{dc}\,d_i/3$
6	1	0	1	$v_{dc}\,d_i/3$	$-\sqrt{3}v_{dc}\,d_i/3$
7	1	1	1	0	0

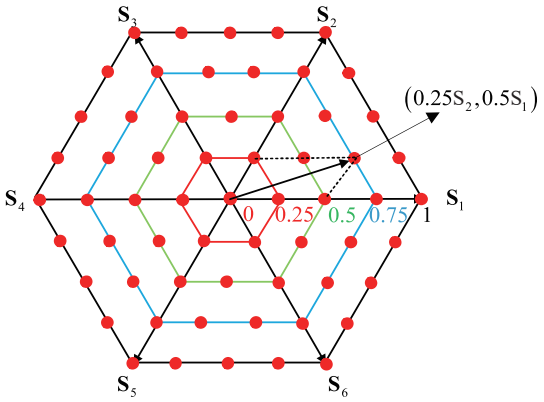

Fig. 5. Virtual voltage vector control set based on duty cycle control.

the action time of $\mathbf{S}_1$ is d_1. Therefore, the basic voltage vectors introduced in Table I are incorporated into the d_i control. Hence, the present study introduces a discrete duty cycle control scheme to streamline the calculation process.

The duty cycle of the motor voltage vector typically ranges from 0 to 1, allowing for active discretization based on this characteristic. For instance, Fig. 5 illustrates the time distribution of a vector divided into intervals of 0, 0.25, 0.5, 0.75, and 1. The figure also displays the distribution and quantity of vector control sets. Each point in Fig. 5 corresponds to different duty cycle control solutions for distinct vectors. Following the solution approach of FCS-MPC, the figure involves iterative calculations for 60 effective vectors (duty cycle control solutions) and zero vectors. Ultimately, the optimal virtual vector with the minimum cost function is chosen as the output for the inverter. However, computing 61 vectors puts a significant computational burden on the chip controller, thus necessitating further optimization of the control set. For example, in Fig. 4, assuming that $\boldsymbol{v}_s$ is the target voltage vector, the optimal voltage vector $\mathbf{S}_2$ and the suboptimal voltage vector $\mathbf{S}_1$ can be obtained during an iterative calculation of the basic effective voltage vector ($d_i \triangleq 1$) of the two-level inverter. So that the sector can be determined and the duty cycle can be optimized in this sector.

A similar design strategy for a discrete duty cycle has been proposed in a previous study [28]. Building upon this method, this paper introduces a novel optimization mechanism aimed

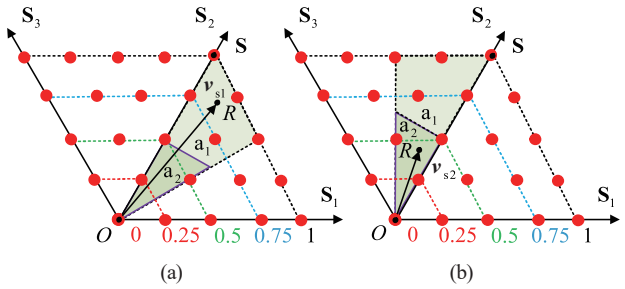

Fig. 6. The optimal vector solution in different target vector sectors. (a) Scenario1, (b) Scenario 2.

at improving the computational efficiency of optimal voltage vector.

B. Optimal Vector Sector Location Strategy

Further, as shown in Fig. 6, it is assumed that the target voltage vectors in two specific control cycles are $\boldsymbol{v}_{s1}$ and $\boldsymbol{v}_{s2}$. For scenario 1, $\mathbf{S}_2$ is the optimal basic voltage vector $\boldsymbol{v}_{opt}^{1st}$, and $\mathbf{S}_1$ is the suboptimal voltage vector $\boldsymbol{v}_{opt}^{2nd}$. For scenario 2, $\mathbf{S}_2$ is the optimal voltage vector $\boldsymbol{v}_{opt}^{1st}$, and $\mathbf{S}_3$ is the suboptimal voltage vector $\boldsymbol{v}_{opt}^{2nd}$. S is the vertex of the optimal basic voltage vector, R is the vertex of the reference voltage vector, and O is the vertex (origin) of the zero vector.

The sector of the target vector can be determined according to the optimal and the suboptimal basic vectors. This sector can be divided into two parts with equal areas, as shown in Fig. 6. Furthermore, the part in the green shadow area close to the optimal basic voltage vector can be used as the search area of the optimal virtual voltage vector. Then, the green shaded area can be further divided into a_1 and a_2 according to the vertical bisector of $\overrightarrow{OS}$. Finally, the search area of the optimal virtual vector can be determined by comparing the distance between $\overrightarrow{OR}$ and $\overrightarrow{SR}$. Here, the amplitude of $\overrightarrow{OR}$ and $\overrightarrow{SR}$ is expressed by the cost value (g_0 and g_{min}) of the zero and optimal basic voltage vectors, respectively. The control region of the optimal vector can be determined in (14).

$$\begin{cases} a_1(d^{1st}, d^{2nd}) = \left\{ \begin{matrix} (0.75,0),\ (1,0),\ (0.5,0.25), \\ (0.75,0.25),\ (0.5,0.5) \end{matrix} \right\} \\ a_2(d^{1st}, d^{2nd}) = \left\{ \begin{matrix} (0,0),\ (0.25,0), \\ (0.5,0),(0.25,0.25) \end{matrix} \right\} \end{cases} \tag{21}$$

Through the above analysis, if the target voltage vector is in the region of a_2 ($g_0 \leqslant g_{min}$), the duty cycle control solution of the optimal basic voltage vector $\boldsymbol{v}_{opt}^{1st}$ and the suboptimal basic voltage vector $\boldsymbol{v}_{opt}^{2nd}$ is {(0,0), (0.25,0), (0.5,0), (0.25,0)}. If the target voltage vector is in the region of a_1 ($g_0 > g_{min}$), the duty cycle control solution of the optimal basic voltage vector $\boldsymbol{v}_{opt}^{1st}$ and the suboptimal basic voltage vector $\boldsymbol{v}_{opt}^{2nd}$ is {(0.75,0), (1,0), (0.5,0.25), (0.75,0.25), (0.5,0.5)}. The control solution of these duty cycles is fixed regardless of the optimal basic vector. So, the vector control set can be expanded to each sector due to the symmetry of the active discrete duty cycle. Since the optimal and suboptimal vectors are known, amplitude computing can significantly reduce the computing time of the chip.

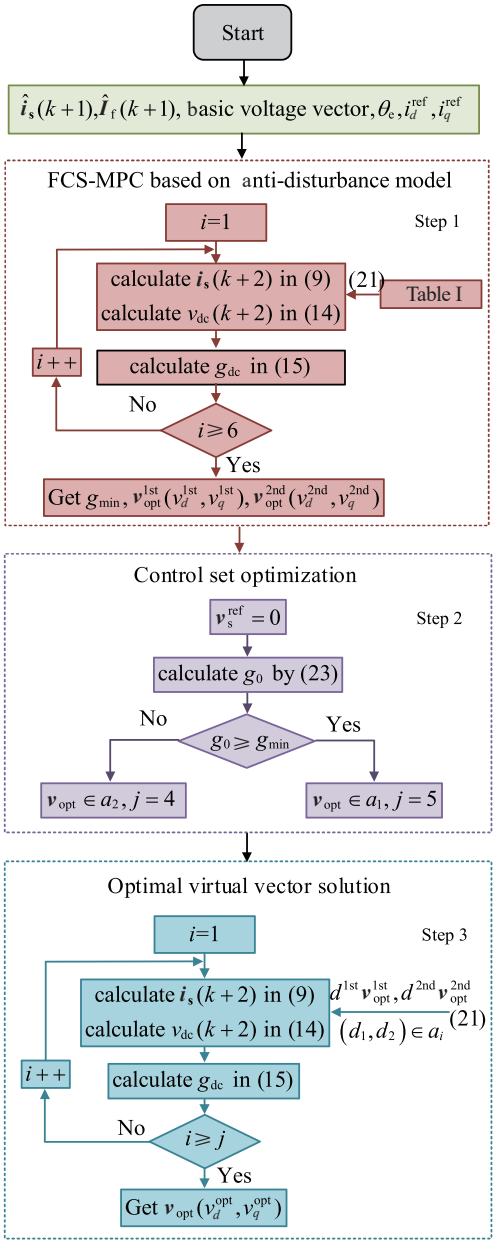

Fig. 7. Control step of DCS-MPDVC.

C. The Calculation Step of the Optimal Virtual Voltage Vector of DCS-MPDVC

The overall algorithm control flow chart is shown in Fig. 7. Step 1 is the same as FCS-MPC, and the calculation amount of the whole control program is mainly affected by this step. In this process, it is necessary to record the optimal and sub-optimal voltage vectors.

Step 1 :

The basic voltage vector must coordinate transformation (22) with the motor rotor position to obtain eight voltage vectors $\boldsymbol{v}_s^{ref}$

$(v_{i,d}, v_{i,q})_{i=1\text{–}6}$ in the dq-axis to facilitate the analysis.

$$T_{2s/2r}(\theta_e)=\begin{bmatrix}\cos\theta_e & \sin\theta_e\\ -\sin\theta_e & \cos\theta_e\end{bmatrix} \tag{22}$$

After coordinate transformation, six dq-axis voltage control solutions are brought into prediction (9), (14) and the cost function (15) to obtain the optimal $\boldsymbol{v}_{opt}^{1st}(v_d^{1st}, v_q^{1st})$ and the suboptimal $\boldsymbol{v}_{opt}^{2nd}(v_d^{2nd}, v_q^{2nd})$ voltage vectors. This step is similar to the FCS-MPC [30].

Step 2 :

The optimization area needs to be further reduced to save computation. First, calculate the cost value of the zero vector according to

$$\begin{aligned} g_0 =& \left[i_d^{ref} - T_s\hat{i}_{df}(k+1) + \hat{i}_d(k+1)\right]^2 \\ &+ \left[i_q^{ref} - T_s\hat{i}_{qf}(k+1) + \hat{i}_q(k+1)\right]^2 \end{aligned} \tag{23}$$

By comparing the size of g_0 and g_{min}, the duty cycle control set is obtained from

$$\begin{cases} \text{if } g_0 \leqslant g_{min} : \boldsymbol{v}_{opt} \in a_2(d^{1st}, d^{2nd}) \\ \text{if } g_0 > g_{min} : \boldsymbol{v}_{opt} \in a_1(d^{1st}, d^{2nd}) \end{cases} \tag{24}$$

Step 3 :

After the duty cycle control set is obtained in step 2, the virtual vector in the dq-axis based on the duty cycle solution (d^{1st}, d^{2nd}) can be obtained through

$$\boldsymbol{v}_s^{ref} = \begin{bmatrix} v_d \\ v_q \end{bmatrix} = \begin{bmatrix} d^{1st}v_d^{1st} + d^{2nd}v_d^{2nd} \\ d^{1st}v_q^{1st} + d^{2nd}v_q^{2nd} \end{bmatrix} \tag{25}$$

$\boldsymbol{v}_s^{ref}$ is calculated by the duty cycle in (18). All voltage vectors $\boldsymbol{v}_s^{ref}$ are evaluated successively via (9), (14) and (15) to obtain the optimal duty cycle (d_{opt}^{1st}, d_{opt}^{2nd}) and corresponding optimal virtual vector $\boldsymbol{v}_{opt}(v_d^{opt}, v_q^{opt})$ that minimizes (15).

D. DCS-MPDVC Overall Control Structure

The DCS-MPDVC's control structure is shown in Fig. 2. $i_d^{ref} = 0$ is used for realizing the SPMSM's current control. Because the time scales of the speed loop and the current loop are inconsistent, the proposed control structure retains the speed loop. Therefore, the reference value of the q-axis current comes from the speed loop controller. The electrical angle θ_e in (22) is obtained by the rotor position θ_r and motor pole pairs P. The inner loop current controller mainly uses the predictive equation, the lumped disturbance observer, the control set (Table I and (21)), the optimization mechanism (Fig. 6), and the cost function (14). After the measured value and estimated value are obtained for (9) and (14), the optimal voltage vector is calculated through the control flow in Fig. 7. The optimal voltage vector can be synthesized by the space vector modulation technology proposed in [31] to act on the motor (the control vector can also be synthesized by the rotor position and SVPWM, which requires more calculation).

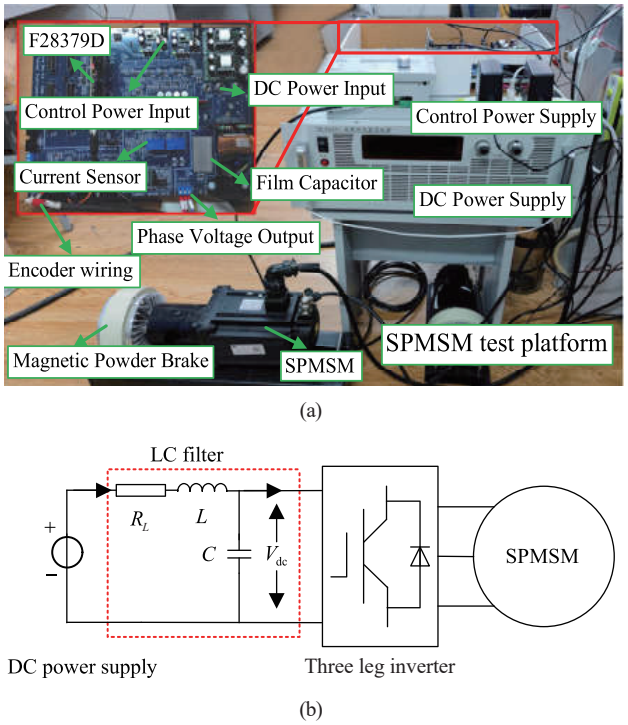

Fig. 8. Experimental hardware platform. (a) Experimental platform, (b) Topology of the experimental platform.

The DCS-MPDVC achieves optimal duty cycle control by implementing a simple judgment mechanism that requires only 4 or 5 additional subset calculation loops. The advantage of this approach is that the subsets are no longer required to undergo coordinate transformation, significantly enhancing both computational efficiency and control accuracy.

IV. Experimental Verification

To verify the proposed control strategy, a hardware experimental platform utilizing a film-capacitor SPMSM drive is employed in this study, as depicted in Fig. 8(a). The experimental setup consists of an SPMSM as the torque output and a magnetic particle brake as the load. The chip utilized is the TMS320F28379D, manufactured by Texas Instruments. The inverter topology entails a two-level voltage source inverter, with its structure depicted in Fig. 8(b). The inverter equipment is also from Texas Instruments (Model: TMDXIDDK379D) and incorporates an IPM module (Model: PS21765). The rectifier is substituted with a DC power supply. The film capacitor is utilized with the parameters referencing the hardware specifications mentioned in [32]. The nameplate parameters of the testing platform are provided in Table II. During the experiment, the controller data is transmitted in real time to the host computer via serial communication, and the host computer plots the experimental results. The switching frequency used in the experiment is 10 kHz (T_s = 0.0001), and the dead time is 5 μs. The experiment's observer bandwidth ω_f is 3000 rad/s, and b is $1/L_{s0}$. The PI controller parameters of the speed loop are K_p = 0.3, K_i = 5, which is designed according to [33]. In addition, unless otherwise specified the motor parameters involved in

TABLE II
EXPERIMENTAL PLATFORM PARAMETERS

Quantity	Symbol	Value
Inverter rated voltage	-	300 V
Inverter rated current	-	8 A
DC-link voltage	V_{dc}	292 V
LC resistance	R_L	0.5 Ω
LC filter inductance	L	3 mH
LC filter capacitance	C	25 μF
Phase resistance	R_{s0}	1.616 Ω
Phase inductance	L_{s0}	11.47 mH
Flux	φ_0	0.175 Wb
Rated current	i_N	4 A
Rated speed	ω_N	1000 rpm
Pole pairs	P	5
Inertia	J	0.0024 kg·m²

TABLE III
CALCULATION TIME OF DIFFERENT CONTROL METHODS

The control method	Time/μs
FCS-MPC	32
MPD2C in [28]	37.5
DCS-MPDVC	32

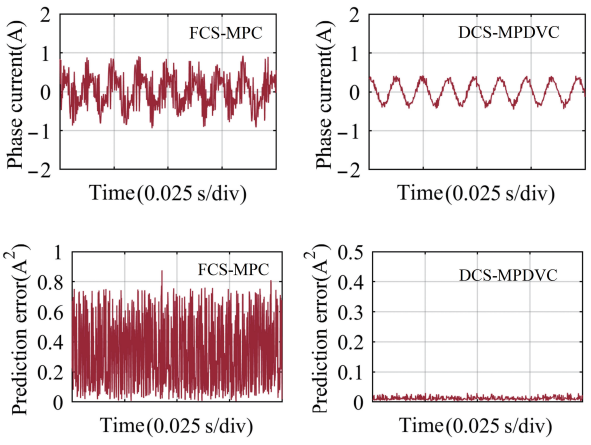

Fig. 9. Experimental results of phase current and predicted error at rated speed.

the controller are the nameplate parameters in Table II.

In this section, the steady-state characteristics of DCS-MPDVC are initially verified. Subsequently, the influence of the anti-interference prediction model on the optimization goal of the current is demonstrated following the enhanced control accuracy achieved by ESO. Finally, the effectiveness of DCS-MPDVC in suppressing DC-link voltage oscillation is evaluated through testing.

A. DCS's Experimental Results of Steady-State Characteristics

The test results of the calculation amount are presented in Table III. In DCS-MPDVC, optimizing the duty cycle does not require coordinate transformation but utilizes scalar calculation, only adding 6 μs to the calculation cycles compared to FCS-MPC. The duty cycle density and programming method proposed in this study align with the MPD2C method introduced in [28]. Moreover, constraints for predicting the DC-link voltage have been implemented. Optimizing the number of duty cycles has significantly enhanced computational efficiency.

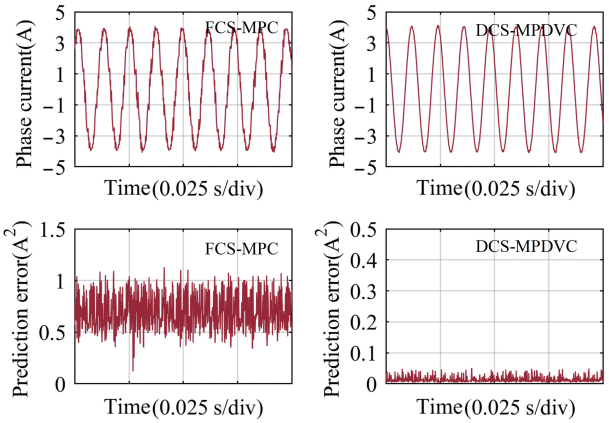

Fig. 10. Experimental results of phase current and predicted error at rated speed.

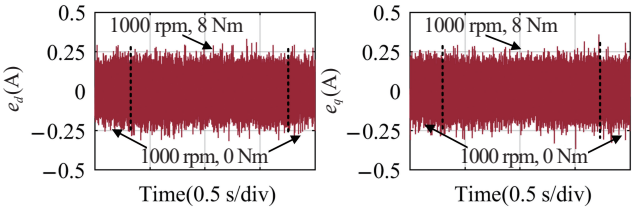

Fig. 11. Experimental results of ESO observation error.

Figs. 9 and 10 are the motor phase current test results and prediction errors under the control of FCS-MPC and DCS-MPDVC. At the rated speed (1000 rpm), the basic voltage vector amplitude is close to the optimal vector amplitude of the motor. However, the FCS-MPC's current distortion is still high because of the significant phase angle error. Because the duty cycle control set in DCS-MPDVC is widely distributed in the whole control area, the zero vector of different control cycles is unnecessary when synthesizing a control vector. Furthermore, the prediction error is slight, so the sinusoidal degree of the phase current is excellent for achieving the control requirements of low current ripple. It can be seen from Figs. 9 and 10 that the prediction error of the DCS-MPDVC is low, which means that the control set accuracy will significantly impact the controller.

B. Experimental Results of the DCS-MPDVC's Robustness

Fig. 11 presents the current observation error of ESO. The *dq*-axis current observation error during the dynamic process is almost negligible. Fig. 12 illustrates the observed disturbance values during the dynamic process, further confirming the excellent dynamic performance of the observer.

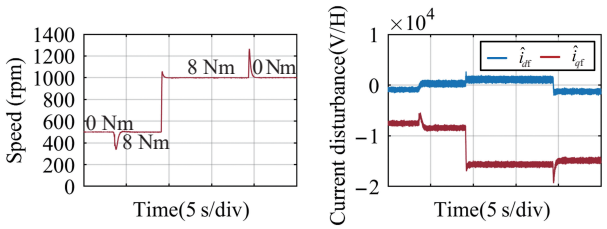

Fig. 12. Experimental results of *dq*-axis observation disturbance under different operating conditions.

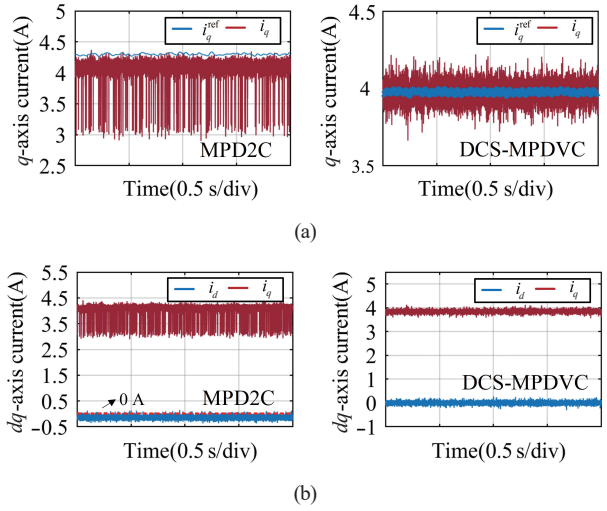

Fig. 13. MPD2C and RDCSMPC's experimental results of the motor *dq*-axis current with artificial parameter error. (a) Motor *q*-axis current and its reference value with artificial parameter error, (b) The motor *dq*-axis is current with an artificial parameter error.

Fig. 13 depicts two sets of comparative tests, and the experiment deliberately introduces an artificial error in the model parameters ($R_s = 2R_{s0}L_s = 2L_{s0}$, $\varphi = 0.5\varphi_0$). In Fig. 13(a), the absence of an anti-disturbance prediction model leads to a steady-state error along with a noticeable current ripple. Conversely, when the anti-interference prediction model is introduced, the steady-state error is eliminated, and the current ripple is significantly reduced. Fig.13(b) depicts the experimental results for the *dq*-axis current. An inaccurate prediction equation leads to non-zero deviation in the *d*-axis current, causing a control error. However, implementing the anti-disturbance prediction model ensures minimal ripples in the *d*-axis and *q*-axis current. This model closely tracks the reference value without any steady-state error.

The experimental results of observation for the inductor current are shown in Fig. 14. An oscilloscope observes the actual value of the inductor current. Through comparison, it can be seen that the steady-state values of the observed value and the actual value are the same, ensuring the system's normal operation.

C. MPDVC's Experimental Results of DC-Link Voltage Oscillation Suppression

Voltage oscillation suppression in a film-capacitor PMSM drive system typically relies on the controller's robustness and control accuracy. The experiment utilizes voltage prediction

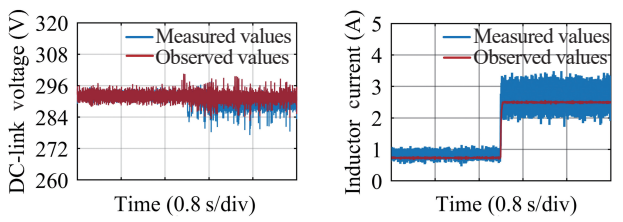

Fig. 14. The DC-link voltage and inductor current observed by the ESO.

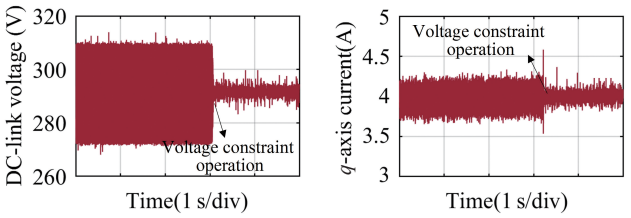

Fig. 15. Experimental results of DC-link voltage and *q*-axis current constraints when the motor operates under the rated working condition.

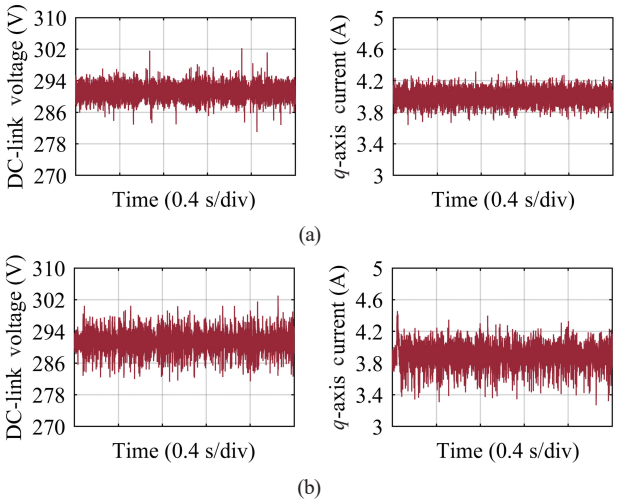

Fig. 16. The comparison experimental results of the stability between the traditional active damping method based on vector control and the proposed DC-link voltage prediction control method: (a) DCS-MPDVC, (b) Active damping compensation.

(14) and a cost function (15). Fig. 15 demonstrates the stabilization effect of DCS-MPDVC on the DC-link voltage during motor operation under rated working conditions. Adding voltage constraints to the cost function enables stable DC-link voltage control.

Fig. 16 shows the experimental results between the active damping method based on the vector control structure and the DC-link voltage constraint method of the control set proposed in [34]. The parameter configuration of the active damping refers to the design method in the paper. It can be seen that, compared with the voltage oscillation suppression achieved indirectly by the active damping, the method proposed in this paper for suppressing the DC-link voltage oscillation is more effective and can also lower the current ripple. These advantages are all due to the direct prediction-constraint structure of the

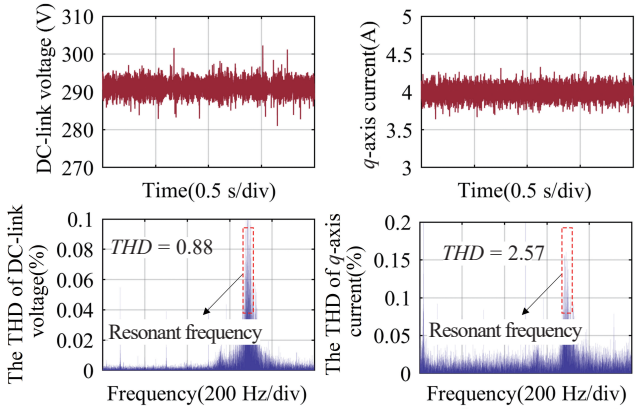

Fig. 17. Experimental results of DC-link voltage and q-axis current based on DCS-MPDVC (the control set is (21)).

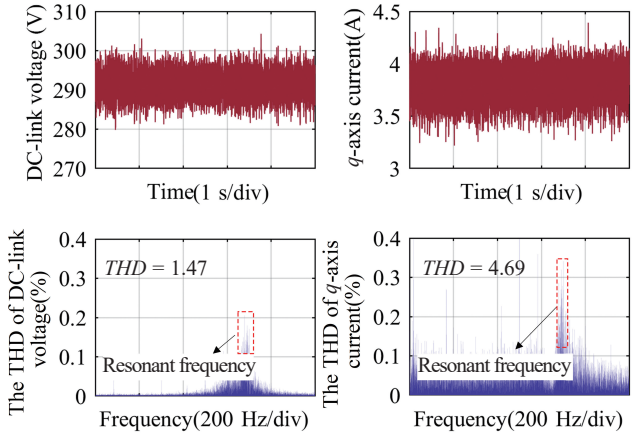

Fig. 18. Experimental results of DC-link voltage and q-axis current based on DCS-MPDVC (control set is (26)).

DC-link voltage.

Figs. 17–19 display the waveforms of the DC-link voltage, q-axis current, and their harmonic analysis under various control conditions. Fig. 16 presents the experimental results of the DCS-MPDVC. Fig. 17 represents the experimental results of the control set (26), while Fig. 18 depicts the experimental results of the prediction model (8).

$$\begin{cases} \text{if } g_0 \leqslant g_{\text{opt}} : v_{\text{opt}} \in a_2, a_2 = \{(0,0)\,(0.5,0)\} \\ \text{if } g_0 > g_{\text{opt}} : v_{\text{opt}} \in a_1, a_1 = \{(1,0)\,(0.5,0.5)\} \end{cases} \tag{26}$$

Compared to Fig. 17, Fig. 18 shows a significant rise in the harmonic content of the DC-link voltage at the oscillation frequency(700 Hz). This observation suggests that decreasing the density of the control set reduces the MPC's constraint ability to constrain the DC-link voltage and dq-axis current. Consequently, this results in a pronounced increase in current ripple and affects the constraint control of the DC-link voltage. Similarly, Fig. 19 exhibits an evident increase in the harmonics of the d-axis current and DC-link voltage compared to Fig. 17. This increase can be attributed to the DCS-MPDVC's inaccurate prediction.

In conclusion, the predictive controller's robustness and the

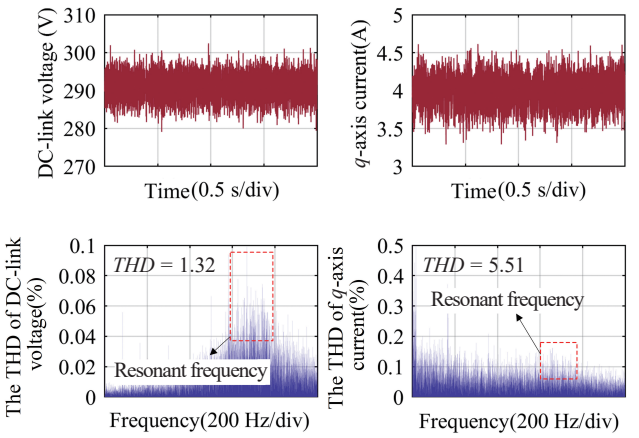

Fig. 19. Experimental results of DC-link voltage stability based on DCS-MPC.

control set's accuracy are essential for multi-objective optimization. The DCS-MPDVC possesses both characteristics, contributing to its superior performance in suppressing current ripple and DC-link voltage oscillation in a film-capacitor PMSM drive system.

V. Conclusion

This paper proposes that DCS-MPDVC solves the problems of significant prediction errors and low constraint accuracy in the film-capacitor permanent-magnet synchronous motor drive system. This method integrates an anti-disturbance prediction model and a duty cycle control set. A parameter configuration method of the ESO based on a low-pass filter is proposed to estimate the lumped disturbance and inductor current. This method effectively solves the estimation problems of unmodeled disturbances and inductor current, improves the prediction accuracy of the DC-link voltage, and reduces physical costs. In addition, a design scheme of the duty cycle control set is introduced, expanding the number of effective virtual voltage vectors from 6 to 60. This scheme includes a simple sector identification principle, which can improve control accuracy within a single control cycle while reducing prediction errors and computational complexity. Experimental results show that the proposed method has better constraint capabilities in the dq-axis and DC-link, making it suitable for the film-capacitor drive system.

References

[1] X. Liu and A. J. Forsyth, "Active stabilisation of a PMSM drive system for aerospace applications," in *Proceedings of 2008 IEEE Power Electronics Specialists Conference*, Rhodes, Greece, Jun. 2008, pp. 283–289.

[2] N. Zhao, G. Wang, B. Li, R. Zhang, and D. Xu, "Beat phenomenon suppression for reduced DC-link capacitance IPMSM drives with fluctuated load torque," in *IEEE Transactions on Industrial Electronics*, vol. 66, no. 11, pp. 8334–8344, Nov. 2019.

[3] Y. Liu, Z. Zhang, H. Guo, Q. Zhang, P. Yang, P. Zhu, and X. Zhuang, "An active DC-link stabilization strategy for permanent magnet synchronous motor drive system based on inverter voltage compensation," in *IEEE/ASME Transactions on Mechatronics*, vol. 27, no. 5, pp. 2786–2795, Oct. 2022.

[4] Z. Ren, D. Ding, G. Wang, B. Li, Q. Wang, G. Zhang, and D. Xu, "Adaptive virtual admittance reshaping-based resonance suppression strategy for PMSM drives with small DC-link capacitor," in *IEEE Transactions on Power Electronics*, vol. 39, no. 3, pp. 3109–3121, Mar. 2024.

[5] J. Huo, N. Zhao, G. Wang, G. Zhang, L. Zhu, and D. Xu, "An active damping control method for reduced DC-link capacitance PMSM drives with low line inductance," in *IEEE Transactions on Power Electronics*, vol. 37, no. 12, pp. 14328–14342, Dec. 2022.

[6] D. Ding, R. Gao, Q. Wang, B. Li, G. Zhang, G. Wang, L. Wu, and D. Xu, "Beatless control strategy based on impedance reshaping for PMSM drives with small DC-link capacitors," in *IEEE Transactions on Industrial Electronics*, vol. 71, no. 7, pp. 6829–6840, Jul. 2024.

[7] I. Won, Y. Cho, and K.-B. Lee, "Predictive control algorithm for capacitor-less inverters with fast dynamic response," in *Proceedings of 2016 IEEE International Conference on Power and Energy (PECon)*, Melaka, Malaysia, Nov. 2016, pp. 479–483.

[8] V. Smidl, S. Janous, and Z. Peroutka, "Improved stability of DC catenary fed traction drives using two-stage predictive control," in *IEEE Transactions on Industrial Electronics*, vol. 62, no. 5, pp. 3192–3201, May 2015.

[9] Z. Zhang, H. Guo, and Y. Liu, "DC-link voltage constraint strategy for DC power supply film-capacitor drive system based on improved model predictive control," in *IEEE Transactions on Industrial Electronics*, vol. 69, no. 10, pp. 9849–9859, 2022.

[10] C. Zheng, T. Dragicevic, and F. Blaabjerg, "Current-sensorless finite-set model predictive control for LC-filtered voltage source inverters," in *IEEE Transactions on Power Electronics*, vol. 35, no. 1, pp. 1086–1095, Jan. 2020.

[11] C. Xue, D. Zhou, and Y. Li, "Finite-control-set model predictive control for three-level NPC inverter-fed PMSM drives with LC filter," in *IEEE Transactions on Industrial Electronics*, vol. 68, no. 12, pp. 11980–11991, Dec. 2021.

[12] D. Q. Dang, M. S. Rafaq, H. H. Choi, and J.-W. Jung, "Online parameter estimation technique for adaptive control applications of interior PM synchronous motor drives," in *IEEE Transactions on Industrial Electronics*, vol. 63, no. 3, pp. 1438–1449, Mar. 2016.

[13] M. Siami, D. A. Khaburi, A. Abbaszadeh, and J. Rodriguez, "Robustness improvement of predictive current control using prediction error correction for permanent-magnet synchronous machines," in *IEEE Transactions on Industrial Electronics*, vol. 63, no. 6, pp. 3458–3466, Jun. 2016.

[14] C. Xia, M. Wang, Z. Song, and T. Liu, "Robust model predictive current control of three-phase voltage source PWM rectifier with online disturbance observation," in *IEEE Transactions on Industrial Informatics*, vol. 8, no. 3, pp. 459–471, Aug. 2012.

[15] A. Andersson and T. Thiringer, "Motion sensorless IPMSM control using linear moving horizon estimation with luenberger observer state feedback," in *IEEE Transactions on Transportation Electrification*, vol. 4, no. 2, pp. 464–473, Jun. 2018.

[16] F. Mwasilu, H. T. Nguyen, H. H. Choi, and J.-W. Jung, "Finite set model predictive control of interior PM synchronous motor drives with an external disturbance rejection technique," in *IEEE/ASME Transactions on Mechatronics*, vol. 22, no. 2, pp. 762–773, Apr. 2017.

[17] Y. Wu and G. Li, "Adaptive disturbance compensation finite control set optimal control for PMSM systems based on sliding mode extended state observer," in *Mechanical Systems and Signal Processing*, vol. 98, pp. 402–414, Jan. 2018.

[18] Y. A.-R. I. Mohamed, "Design and implementation of a robust current-control scheme for a PMSM vector drive with a simple adaptive disturbance observer," in *IEEE Transactions on Industrial Electronics*, vol. 54, no. 4, pp. 1981–1988, Aug. 2007.

[19] R. Madonski, G. Herbst, and M. Stankovic, "ADRC in output and error form: connection, equivalence, performance," in *Control Theory and Technology*, vol. 21, no. 1, pp. 56–71, Feb. 2023.

[20] Z. Zhang, X. Wang, and J. Xu, "Robust amplitude control set model predictive control with low-cost error for SPMSM based on nonlinear extended state observer," in *IEEE Transactions on Power Electronics*, vol. 39, no. 6, pp. 7016–7028, Jun. 2024.

[21] X. Wu, J. Kang, M. Yang, T. Wu, and S. Huang, "Model-free deadbeat predictive current control for SPMSM based on adaptive gain extended state observer," in *IEEE Transactions on Transportation Electrification*, pp. 1–1, 2024.

[22] J. Chen, Y. Fan, M. Cheng, Q. Zhang, and Q. Chen, "Parameter-free ultralocal model-based deadbeat predictive current control for PMVMs using finite-time gradient method," in *IEEE Transactions on Industrial Electronics*, vol. 70, no. 6, pp. 5549–5559, Jun. 2023.

[23] Y. Liu, S. Cheng, Y. Zhao, J. Liu, and Y. Li, "Optimal two-vector combination-based model predictive current control with compensation for PMSM drives," in *International Journal of Electronics*, vol. 106, no. 6, pp. 880–894, Jun. 2019.

[24] Z. Zhou, C. Xia, Y. Yan, Z. Wang, and T. Shi, "Torque ripple minimization of predictive torque control for PMSM with extended control set," in *IEEE Transactions on Industrial Electronics*, vol. 64, no. 9, pp. 6930–6939, Sept. 2017.

[25] Z. Ma, S. Saeidi, and R. Kennel, "FPGA implementation of model predictive control with constant switching frequency for PMSM drives," in *IEEE Transactions on Industrial Informatics*, vol. 10, no. 4, pp. 2055–2063, Nov. 2014.

[26] Y. Zhang, H. Jiang, and H. Yang, "Model predictive control of PMSM drives based on general discrete space vector modulation," in *IEEE Transactions on Energy Conversion*, vol. 36, no. 2, pp. 1300–1307, Jun. 2021.

[27] Y. Wang, X. Wang, W. Xie, F. Wang, M. Dou, R. M. Kennel, R. D. Lorenz, and D. Gerling, "Deadbeat model-predictive torque control with discrete space-vector modulation for PMSM drives," in *IEEE Transactions on Industrial Electronics*, vol. 64, no. 5, pp. 3537–3547, May 2017.

[28] Z. Zhou, C. Xia, T. Shi, and Q. Geng, "Model predictive direct duty-cycle control for PMSM drive systems with variable control set," in *IEEE Transactions on Industrial Electronics*, vol. 68, no. 4, pp. 2976–2987, Apr. 2021.

[29] T. Dragicevic, "Dynamic stabilization of DC microgrids with predictive control of point-of-load converters," in *IEEE Transactions on Power Electronics*, vol. 33, no. 12, pp. 10872–10884, Dec. 2018.

[30] M. Aguirre, S. Kouro, C. A. Rojas, J. Rodriguez, and J. I. Leon, "Switching frequency regulation for FCS-MPC based on a period control approach," in *IEEE Transactions on Industrial Electronics*, vol. 65, no. 7, pp. 5764–5773, Jul. 2018.

[31] I. Osman, D. Xiao, K. S. Alam, S. Shakib, M. P. Akter, and M. F. Rahman, "Discrete space vector modulation-based model predictive torque control with no suboptimization," in *IEEE Transactions on Industrial Electronics*, vol. 67, no. 10, pp. 8164–8174, 2020.

[32] N. Zhao, G. Wang, D. Ding, G. Zhang, and D. Xu, "Impedance based stabilization control method for reduced DC-link capacitance IPMSM drives," in *IEEE Transactions on Power Electronics*, vol. 34, no. 10, pp. 9879–9890, Oct. 2019.

[33] L. Harnefors, K. Pietilainen, and L. Gertmar, "Torque-maximizing field-weakening control: design, analysis, and parameter selection," in *IEEE Transactions on Industrial Electronics*, vol. 48, no. 1, pp. 161–168, Feb. 2001.

[34] D. Wang, K. Lu, P. O. Rasmussen, L. Mathe, Y. Feng, and F. Blaabjerg, "Voltage modulation using virtual positive impedance concept for active damping of small DC-link drive system," in *IEEE Transactions on Power Electronics*, vol. 33, no. 12, pp. 10611–10621, Dec. 2018.

Zhenrui Zhang was born in 1994 in Qingdao, Shandong Province, China. He received the B.S. degree in Engineering from Yantai University, in 2017. From 2017 to 2023, he pursued a consecutive master's and doctoral program at Dalian Maritime University in Dalian, China, and obtained the Ph.D. degree in engineering in 2023. He works as a full-time researcher at the Marine Equipment and Technology Institute of Jiangsu University of Science and Technology.

His research interests include permanent magnet synchronous motor drive control, model predictive control, thin film capacitor drive systems, and shipborne electric propulsion systems.

Jing Xu is an associate professor of mechatronic engineering at the Marine Equipment and Technology Institute, Jiangsu University of Science and Technology, Zhenjiang, China. He received his Ph.D. degree from the China University of Mining and Technology, Xuzhou, China 2018.

His research interests include signal processing, pattern recognition, and intelligent systems.

Xingyu Wang was born in 1989 in Jinzhou, Liaoning Province, China. He received the B.S. degree in Electrical Engineering and Automation and the M.S. degree in Electrical Engineering from Liaoning University of Engineering and Technology in 2014 and 2017, respectively. He received his Ph.D. degree in power electronics and electric drive from Northeastern University, Liaoning, China, in 2022. He is with the Marine Equipment and Technology Institute, Jiangsu University of Science and Technology, China.

His research interests include robotic manipulator motion control, server drive systems, intelligent manufacturing, sliding electrical contact, and basic theory of electrical equipment.

Qingya Zhang, born in 1990 in Lianyungang, Jiangsu Province, China. He received the B.S. degree in Engineering from Nanjing Institute of Technology, in 2014, and the M.S. degree in engineering from Jiangsu University of Science and Technology, in 2017. From 2017 to 2022, he studied at Huazhong University of Science and Technology as a Ph.D. student and obtained the Ph.D. degree in engineering in 2022. He works as a full-time researcher at the Marine Equipment and Technology Institute of Jiangsu University of Science and Technology.

His research interests include intelligent servo drive system and mechanical engineering.